

# Geometrical-phase lens based optical system for the spin-splitting of vector beams

Aarón Cofré<sup>1</sup>, Asticio Vargas<sup>2</sup>, Fabián A. Torres-Ruiz<sup>2</sup>, María del Mar Sánchez-López<sup>3,\*</sup> and Ignacio Moreno<sup>1</sup>

1. TecnOPTO Group. Departamento de Ciencia de Materiales, Óptica y Tecnología Electrónica, Universidad Miguel Hernández de Elche, 03202 Elche, Spain.
2. Departamento de Ciencias Físicas, Universidad de La Frontera, Temuco, Chile.
3. TecnOPTO Group. Instituto de Bioingeniería, Departamento Física y Arquitectura de Computadores, Universidad Miguel Hernández, 03202 Elche, Spain.

\* Corresponding author: [mar.sanchez@umh.es](mailto:mar.sanchez@umh.es)

## Abstract:

In this work, we present a new optical lens system based on a polarization directed flat lens (geometric phase lens) designed to provide circular polarization split focusing in two real foci located at two different axial planes. We find the conditions to obtain two real back focal planes of the system, and the same focal length of opposite sign. In this situation, the system acts as a bifocal SAM split system with equal scale for both real foci. We experimentally demonstrate the optical spin dependent dual focus effect of the system. Then, we illuminate the system with vortex and vector beams generated by a  $q$ -plate and provide theoretical explanation within the Jones matrix formalism for the different orbital angular momentum (OAM) and spin angular momentum (SAM) states experimentally observed at the two focal planes. Finally, we show the interference of the two split focused components of the vector beam at the intermediate plane between the two focal planes. The resulting spiral interference pattern indicates the sign and value of the vector beam's topological charge. It can also be used to identify the vector beam of a given charge by the shift on the interference fringes. Therefore, the optical system can be useful as a new tool for analyzing OAM and SAM beams.

## Highlights:

- We combine a geometric phase lens and a telescope to produce an optical system with two polarization controlled real foci with equal magnification.
- We apply it to characterize vortex beams and vector beams, splitting longitudinally the circular polarization components and focusing them into different axial planes.
- We show the polarization interference pattern obtained at an intermediate plane, which easily reveals the difference and relative sign of the vector beam's topological charge at each circular component.

- This interference pattern can be used to identify the vector beam of a given order through the relative phase between the RCP and LCP components, which is clearly visible in the shift of the interference pattern at the intermediate plane.

**Keywords:** Vector Beams; Geometric Phase Lens; Polarization Interference.

## 1. Introduction

In recent times there has been a great interest in developing geometric phase (also known as Pancharatnam-Berry phase) diffractive optical elements (GP-DOE). These thin optical elements allow reducing the size of the optical systems, while maintaining high efficiency [1,2]. These GP-DOEs are basically half-wave retarders (HWR) where the angle of the fast (or slow) axis follows a given spatial pattern  $\phi(\mathbf{r})$ , where  $\mathbf{r}$  denotes the spatial coordinate in the plane of the GP-DOE. When the GP element is illuminated with right circularly polarized (RCP) light, the output beam is left circularly polarized (LCP), and gains a phase  $2\phi(\mathbf{r})$ . When illuminated with the opposite circular polarization (LCP), the output is RCP and the opposite phase  $-2\phi(\mathbf{r})$  is acquired. More complex designs involve not only controlling the orientation of the spatial retarder at each position, but also the spatial variation of an additional phase, thus allowing to encode two independent phase functions onto the two circular polarizations [3].

Such GP-DOE can be fabricated following two main techniques: 1) via nanostructuring metasurfaces [4,5], and 2) via photo-aligning liquid-crystal materials [1]. Whilst the first technique provides optical devices with structured birefringence and much higher light intensity tolerance, thus making possible the use of high power lasers, the second technique provides material birefringence and much more cost effective. In addition, liquid-crystal based SP elements can be made tunable with voltage and therefore useful for operation and different wavelengths [6,7].

In general, compact thin optical GP elements such as lenses, gratings, and holograms have been reported. In this work we will deal with standard GP-DOEs with  $\pi$  retardance at the operating wavelength (HWR plates). One such popular GP-DOE is the  $q$ -plate [8]. In this case the optical axis space distribution follows  $\phi(x,y)=q\theta$ , where  $\theta$  is the azimuthal angle,  $\tan(\theta)=y/x$ . GP-DOE  $q$ -plates have become very popular since they transfer orbital angular momentum (OAM) of charge  $\pm 2q\hbar$  per photon to circularly polarized light (the sign depends whether input light is RCP or LCP). This is an additional angular momentum added to the spin angular momentum (SAM) of  $\sigma\hbar$  per photon that is associated to circularly polarized states ( $\sigma=\pm 1$  depending on the helicity of the circular polarization).  $Q$ -plates can also be used to generate higher-order cylindrically polarized light (vector beams). When they are illuminated with a uniform polarization state, the output is a vector beam with the same ellipticity as the input beam, but with an orientation that follows the azimuth angle [7,9]. Since  $q$ -plates are flat elements, they allow the generation of vector beams in very compact systems, thus being an advantage over other approaches that require SLMs [10], double-wedge birefringent prisms [11], or axicon elements [12].

Nowadays,  $q$ -plates are actually commercially available at various suppliers, like Edmund Optics, Thorlabs or Arcoptix.

A second type of commercially available GP-DOEs are known as metalenses (when made of metamaterials) or polarization directed flat lenses (when fabricated with liquid crystals). In this case, the optical axis orientation follows the characteristic phase of a lens; namely, proportional to the square of the radial coordinate and inversely proportional to the focal length. For these lenses, one input circular polarization results in a converging beam, while the orthogonal circular polarization results in a diverging beam [13]. The encoded focal length in each case is  $\pm f$ , thus acting as a polarization beam splitter, separating the circular states. Such lenses were demonstrated in Refs. [13-15], and they have been applied to create novel optical systems such as new spectrometers [16], or new polarized-based zoom lenses [17].

In this work, we combine and make the most of the properties of these two kinds of GP-DOEs described above. We use a GP lens to build an optical system that splits the circularly polarization components (or SAM components) of the input beam onto two different foci located at different axial distances. This system is composed of the GP-DOE lens followed by a telescopic system. The purpose of the telescopic system is to image the two back focal planes provided by the GP lens (one real and the other virtual) onto two real foci, both with the same magnification. In some cases, before the GP lens we place a  $q$ -plate to generate vector beams that will impinge on the GP lens.

Since the flat lens splits the circular polarization components of the input beam, this optical system directly allows the analysis of the incoming beam in the basis of circular states. This is very interesting for analysing cylindrically polarized beams, since these beams are the superposition of RCP and LCP vortex beams with opposite OAM. The two foci of the flat-lens based optical system directly show the content of the incoming beam in this basis. In addition, the intermediate planes between the two foci reveal a spiral interference pattern when a linear polarizer analyzer is added to the system, which serves to identify the sense of rotation of the input vector beam.

These spin splitting properties could be exploited in OAM-based optical communications [18], and in beyond OAM optical communications using vector beams where the information is encoded in the polarization distribution [19,20]. Hence, these spin-splitting properties could be used in building decoding schemes similar to that in [21]. Also, the proposed optical set-up could benefit the research on the spin-Hall effect of light, which has been proposed for optical manipulation and trapping [22] and where a longitudinal spin splitting using a spatial light modulator was recently reported [23].

The paper is organized as follows: after this introduction, section 2 describes the GP-DOE properties, and the proposed optical set-up is explained in section 3. Experimental results are provided in section 4 for different input beams: beam with different uniform polarizations, but also vector beams generated by  $q$ -plates. Finally, the conclusions of the work are given in section 5.

## 2. Geometric-phase diffractive optical elements

A standard GP-DOE is basically a HWR whose fast axis orientation follows a given function  $\phi(\mathbf{r})$  of the space coordinates in the retarder's section. According to the Jones matrix formalism, the Jones matrix describing this element is given by [8]:

$$\mathbf{M}_{\text{GP}}[\phi(\mathbf{r})] = \mathbf{R}(-\phi) \cdot \mathbf{HWR} \cdot \mathbf{R}(+\phi) = \begin{pmatrix} \cos(2\phi) & \sin(2\phi) \\ \sin(2\phi) & -\cos(2\phi) \end{pmatrix} \quad (1)$$

where  $\mathbf{R}(\phi) = [\cos(\phi), \sin(\phi); -\sin(\phi), \cos(\phi)]$  stands for the 2x2 rotation matrix, and  $\mathbf{HWR} = \text{diag}[1, -1]$  is the Jones matrix for the aligned HWR. Note that in this relation  $\phi$  is a spatially variant function  $\phi(\mathbf{r})$ .

When such a GP-DOE is illuminated with circularly polarized light, the output beam is given by:

$$\mathbf{M}_{\text{GP}}(x, y) \cdot \mathbf{C}_{\sigma} = \exp(2i\sigma\phi) \mathbf{C}_{-\sigma} \quad (2)$$

where the normalized Jones vectors for the circular states are written following the convention in [24] as:

$$\mathbf{C}_{\sigma} = \frac{1}{\sqrt{2}} \begin{pmatrix} 1 \\ \sigma i \end{pmatrix} \quad (3)$$

with  $\sigma = +1$  for RCP polarization and  $\sigma = -1$  for LCP polarization.

Equation (2) shows that a GP-DOE flips the circular polarization (as expected of a HWR), but also imparts a phase term  $\exp(2i\sigma\phi)$  whose sign depends on the helicity of the input circular polarization. If the GP-DOE is a  $q$ -plate, the axis orientation pattern follows a helical phase  $\phi = q\theta$ ,  $q$  being the  $q$ -value and  $\theta$  the azimuthal coordinate, while for a GP lens the axis orientation pattern follows a quadratic phase function,  $\phi = \pi r^2 / \lambda f$ , with  $f$  denoting the lens focal length,  $\lambda$  the wavelength, and  $r$  the radial coordinate.

Figure 1 shows the action of these two GP elements on the RCP/LCP polarization components. The  $q$ -plate device imparts an orbital angular momentum (OAM) with topological charge  $\ell = 2\sigma q$  to the input beam, where the sign depends on the input circular polarization (Fig. 1(a)). When illuminating with linearly polarized light, the  $q$ -plate generates a cylindrically polarized light beam (vector beam). In the case of the GP lens (Fig. 1(b)), it acts as a converging lens for one circular polarization, while it acts as a diverging lens for the opposite circular polarization. For linearly polarized light, it acts as a bifocal lens splitting the incoming beam intensity evenly between the two foci.

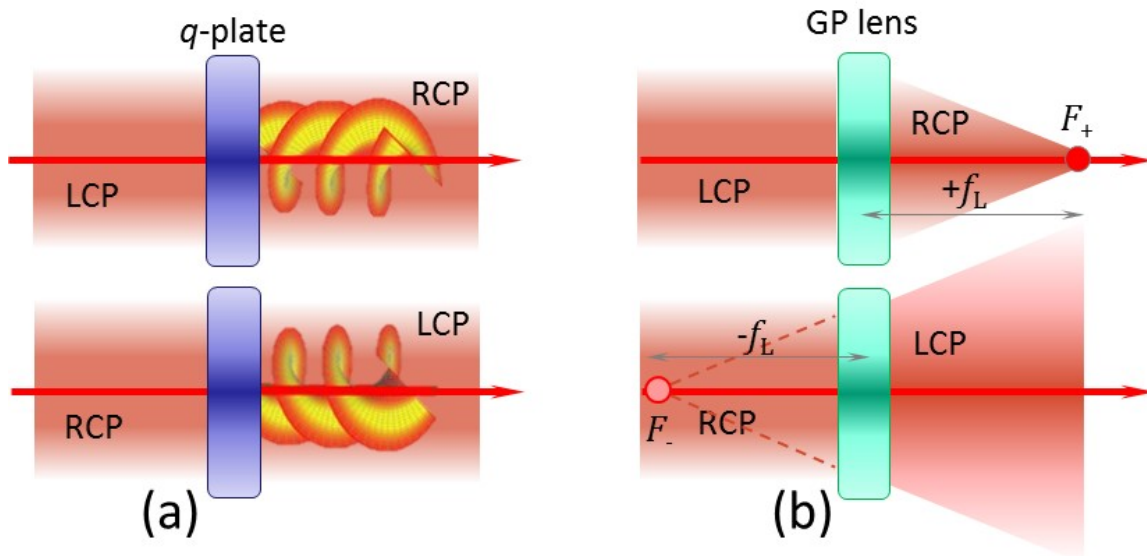


Fig. 1. Action of the two GP elements used in this work. RCP and LCP stand for left and right circularly polarized light. (a) A  $q$ -plate transfers OAM with charge of opposite sign for RCP/LCP light. (b) A GP lens converges (diverges) for RCP (LCP) light.

Next, we combine the action of these two GP-DOE components. The GP lens is used to split the circular polarization components of a vector beam generated by a  $q$ -plate.

### 3. Optical system

The key element in our experiment is a GP lens from Edmund Optics, known as a polarization directed flat lenses. These are polymerized liquid-crystal thin-films, approximately 0.45 mm thick, with an effective area of  $2.5 \times 2.5 \text{ cm}^2$ , and a nominal focal length of  $f_L = \pm 100 \text{ mm}$ . Figure 2 illustrates the dual focus property of these lenses. In Fig. 2(a) we placed the lens right on top of a piece of paper with a text written. Because the lens is flat it can be completely placed on the paper and a single image is observed. In Fig. 2(b) we separate the lens from the text, and two images are visible, with two different magnifications. These images are circularly polarized with opposite circular polarizations. Chromatic aberration is observed.

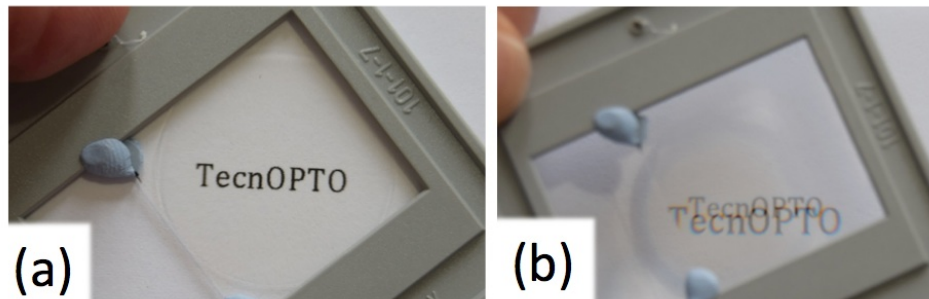


Fig. 2. A text on a paper viewed through the GP flat lens: (a) Lens directly placed on the text; (b) The lens is separated from the text in order to show the dual image property with different magnification.

Figure 3 shows a scheme of the optical system where we exploit the properties of this lens. We use a 632.8 nm wavelength He-Ne laser. The beam is spatially filtered, and collimated, with a diameter of approximately 2". A polarization state generator (PSG) composed by a linear polarizer (LP) and a quarter-wave retarder (QWR) is introduced in order to generate an arbitrary input state of polarization. In some of the experiments, the PSG also includes a  $q$ -plate device behind the QWR, in order to illuminate the optical system with a vortex beam or a cylindrically polarized beam (vector beam). The  $q$ -plate charge and the state of polarization incident on the  $q$ -plate will determine the resulting vector beam [7,9]. We use commercial  $q$ -plates from Thorlabs, the so-called vortex half-wave retarders of values  $q=1/2$  (model WPV10L-633) and  $q=1$  (model WPV10-633).

This input beam illuminates the GP lens, which generates two foci, one real and one virtual. In order to obtain two real foci, we incorporate a telescopic system behind the GP lens, composed by two positive lenses with focal lengths of approximately  $f_1=165$  mm and  $f_2=175$  mm. Figure 3 illustrates some ray tracing. This telescopic system transforms the real and virtual foci of the GP lens into two real foci behind the telescopic system, both with the same magnification given by  $M=f_2/f_1=1.06$ . The appendix at the end of the paper includes the discussion of the conditions to achieve two real foci at the output of the optical system. In the experiments shown hereafter, we selected the GP lens located a distance of 10.5 cm from lens  $L_1$ , so the focus  $F_+$  is located before the first lens of the telescope. The two final foci  $F_1$  and  $F_2$  are located at distances of approximately  $Y_-=13$  cm and  $Y_+=35$  cm, which are in good agreement with the expected distances (11.9 cm and 34.4 cm respectively).

In front of the CCD detector (Basler model Scout with 1390×1038 pixels, 4.65×4.65  $\mu\text{m}^2$  pixel size and an effective area of 6.5×4.8  $\text{mm}^2$ ) we also introduce a polarization state analyzer (PSA) (not shown in the figure for simplicity), again composed by a quarter-wave plate and a linear polarizer. We use this PSA to capture different polarizations at the system's output.

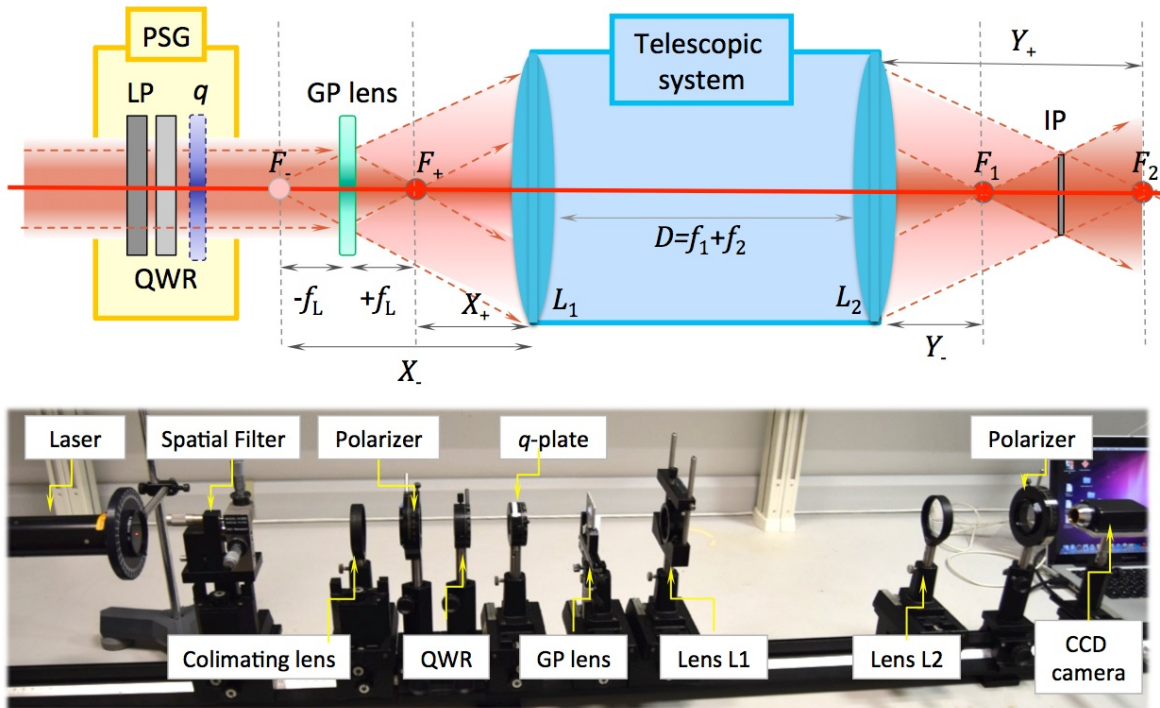


Fig. 3. Top: scheme of the optical system. PSG stands for the polarization state generator composed by a linear polarizer (LP), a quarter-wave retarder (QWR) and, eventually, a  $q$ -plate ( $q$ ). The GP lens provides two foci, one real ( $F_+$ ) and one virtual ( $F_-$ ). A telescopic system composed by lenses  $L_1$  and  $L_2$  provides the two real foci ( $F_1$  and  $F_2$ ) with the same magnification. IP is the intermediate plane between the two foci where the two beams have the same diameter.  $X$  and  $Y$  denote the telescope's object and image distances for the two foci. Bottom: picture of the optical system with indication of the different elements.

## 4. Experiments

In this section we describe the set of experiments we performed. First, we consider the focalization of a single laser beam passing through the GP lens system and analyze the dependence at each focal plane on the input state of polarization, and verify that the two foci are circularly polarized with opposite helicity. Second, we study the behaviour of light passing through a  $q$ -plate to generate a vector beam that is the input to the GP lens-based optical system, and again analyze the result at the resulting foci. We analyze cases with a single  $q$ -plate, or with a combination of two  $q$ -plates, manipulating the addition or subtraction of their  $q$ -values according to reference [25]. Finally, in a third measurement we study the interference pattern that is observed in the intermediate plane between the two foci.

### 4.1 Characterizing the two foci of the GP lens

In this first case we analyze the two focal spots of the GP lens. For this purpose, the GP lens is illuminated with three states of polarization: a linear polarization, and the RCP and LCP states. The CCD camera is displaced longitudinally to capture both focal spots. Figure 4 shows the corresponding experimental captures at planes  $F_1$  and  $F_2$  in Fig. 3 for these

three input polarization states. In addition, for each case, we capture three situations: when no analyzer is placed before the CCD and when the RCP and LCP analyzers are placed.

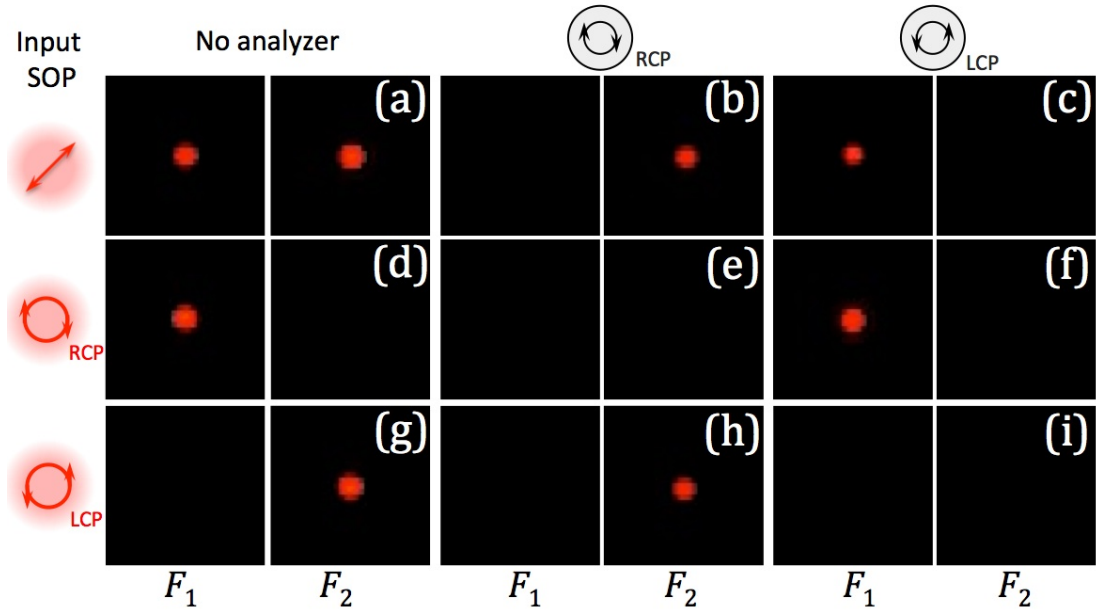


Fig. 4. Experimental captures at planes  $F_1$  and  $F_2$  when the system is illuminated with different input uniform states of polarization (SOP): linear polarization (a-c), with RCP polarization (d-f) and with LCP polarization (g-i). For each case, the two foci are characterized without analyzer (two left columns), with a RCP analyzer (two central columns) and with a LCP analyzer (two right columns).

If the system is illuminated with linearly polarized light (Fig. 4(a)), both foci appear with the same intensity in the absence of analyzer. Note how the two foci appear with the same magnification, thanks to the use of the telescopic system. If a circular analyzer is included before the CCD, then one of the two foci disappears. Namely,  $F_1$  when the RCP analyzer is employed (Fig. 4(b)), and  $F_2$  when the LCP analyzer is employed (Fig. 4(c)). This reveals that the two foci have opposite circular polarizations.

On the contrary, when the system is illuminated with circularly polarized light, only one focus is obtained:  $F_1$  for input RCP polarization (Fig. 4(d)), and  $F_2$  for input LCP polarization (Fig. 4(g)). Again, when circular analyzers are included before the CCD detector, the focus is fully transmitted or fully absorbed depending on the foci. Note the inversion of the output circular polarization in comparison to the input circular polarization caused by the half-wave retardance of the GP lens.

These results thus prove the spin splitting characteristics of the GP lens. The intensity of each foci is proportional to the circular RCP and LCP components of the input beam. Thus serving as an interesting alternative to polarization beam splitters, which usually split the two linear orthogonal components.

#### 4.2 GP lens illuminated with cylindrically polarized light

Next, we add a  $q$ -plate in the PSG system, in order to illuminate the GP lens with a cylindrically polarized light beam. Figures 5 and 6 show results equivalent to those in Fig. 4, but when a  $q$ -plate of  $q=1/2$  and  $q=1$  is included in the PSG, respectively.

When the  $q$ -plate is illuminated with polarized light, it is well known to generate a vector beam or cylindrically polarized beam [6,7,9]. This kind of beam can be viewed as the superposition of an RCP and an LCP beam with helical phases  $\pm 2q\theta$  of opposite sign [26], and they can be represented in the higher-order Poincaré sphere [27]. Thus, when illuminated with a beam of uniform polarization and no OAM content, the  $q$ -plate generates two vortex beams onto the two circular polarization components with charges given by  $\ell = \pm 2q$  which, for the two  $q$ -plates used in this work, they take values  $\ell = \pm 1$  and  $\ell = \pm 2$  respectively. If the input beam already contains topological charge, the  $q$ -plate adds and subtracts the above-mentioned charges to the input one on each circular polarization component. The resulting beam is called a vortex vector beam, and it is represented in the hybrid higher-order Poincaré sphere [28].

Figures 5 and 6 show results equivalent to those in Fig. 4, but when a  $q$ -plate of  $q=1/2$  and  $q=1$  is included in the PSG, respectively. We generate exactly the same three states of polarization as in Fig. 4, i.e. a linear state at  $45^\circ$ , and the two circular states. These states illuminate the  $q$ -plate and generate the corresponding vector beam drawn in the left column of Figs. 5 and 6. These vector beams are now analyzed with the lens system. The GP lens splits the two components of these cylindrically polarized light beams. The results in Figs. 5 and 6 evidence that each circular component is now a vortex beam since they contain a singularity at each focal spot, which now adopts the typical “doughnut” shape. Note that the singularity has the same size at both focal planes, thus indicating the same absolute value of the topological charge in each circular polarization component. Also note that, as expected, the singularity becomes greater when we use the  $q$ -plate with  $q=1$  (Fig. 6) in comparison to the case with  $q=1/2$  (Fig. 5).

Let us note that this simple direct identification and comparison of the topological charge in each foci is only possible because the magnification is the same at both planes, thanks to the use of the telescopic system. This is not the case for the RCP/LCP longitudinal splitting reported in [23], which has a different magnification at each foci.

When the  $q$ -plate is illuminated with circularly polarized light (second and third rows in Figs. 5 and 6) then only one focus is obtained. However, since the  $q$ -plate is a GP element, it flips the initial helicity of the circular polarization, and therefore these foci appear exchanged with respect to the input circular polarization state, in comparison to the initial case in Fig. 4. Namely, the results obtained for input RCP in Figs. 5 and 6 (2<sup>nd</sup> row) are equivalent to those obtained for input LCP in Fig. 4 (3<sup>rd</sup> row); and similarly for input LCP in Figs. 5 and 6 with respect to input RCP in Fig. 4.

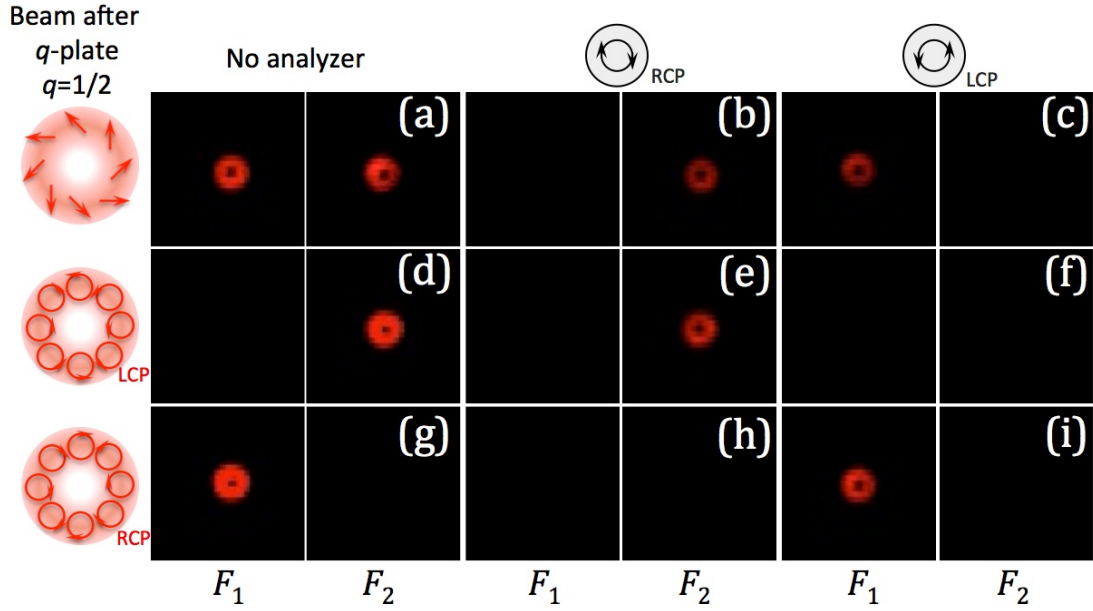


Fig. 5. Experimental captures at planes  $F_1$  and  $F_2$  when the when the PSG system includes a  $q$ -plate of  $q=1/2$ . The vector beam incident on the GP lens is drawn on the left column. For each case, the two foci are characterized without analyzer (a,d,g), with a RCP analyzer (b,e,h) and with a LCP analyzer (c,f,i).

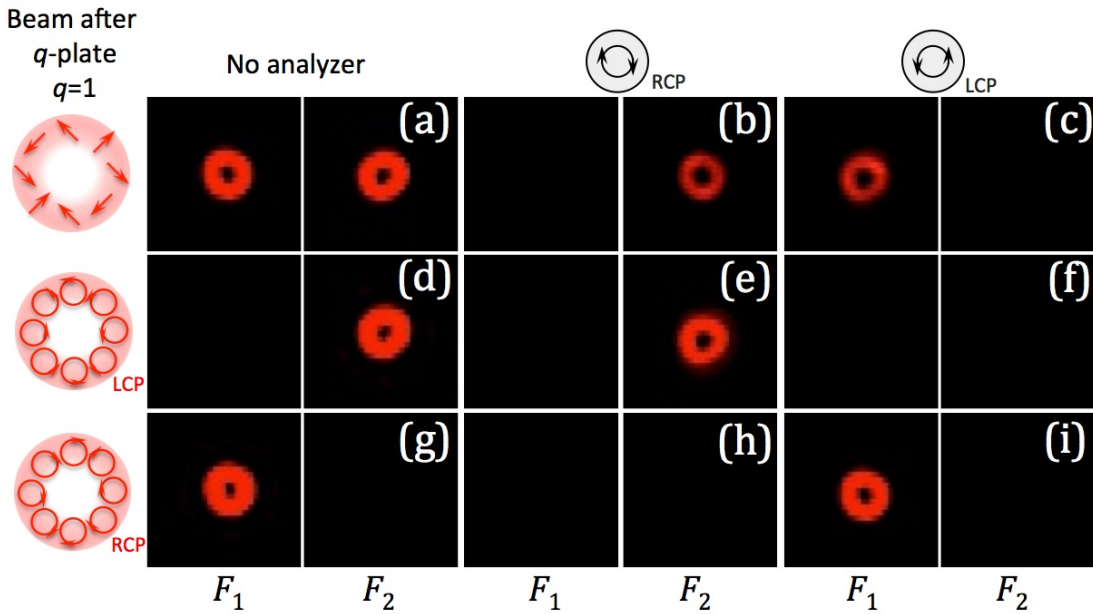


Fig. 6. Experimental captures at planes  $F_1$  and  $F_2$  when the when the PSG system includes a  $q$ -plate of  $q=1$ . The vector beam incident on the GP lens is drawn on the left column. For each case, the two foci are characterized without analyzer (a,d,g), with a RCP analyzer (b,e,h) and with a LCP analyzer (c,f,i).

#### 4.3 Interference of the focused vortex components of a vector beam

These previous results reveal the different topological charge of each circular polarization component. However, the difference in their sign is not shown since positive and negative topological charges yield a doughnut focus of exactly the same diameter.

The sign difference can be indeed shown in a plane where the two beams interfere. For that purpose, we shift the detector to the intermediate plane IP in Fig. 3, where both beams have the same diameter. This way, if the two circular polarization components have the same weight in the input beam, the two focused beams will show equal intensity and their interference will show maximum contrast. However, the two circular states are orthogonal and therefore they do not interfere, at least not in the classical way as intensity fringes, although the local spatial variations of the state of polarization can be viewed as some kind of interference [29]. In order to obtain interference fringes, we put a linear polarizer in front of the CCD detector.

The experimental results are presented in Fig. 7. Here, the input beam was linearly polarized at  $45^\circ$ , so that both circular components have the same intensity. In Fig. 7(a) no analyzer is included before the CCD detector and a constant uniform intensity is observed, since the two focused beams do not interfere. In Fig. 7(b), a linear polarizer analyzer is included at  $45^\circ$ , and now the interference fringes show the quadratic radial phase difference between the two beams due to the axial different location of their respective foci.

In the other cases displayed in Fig. 7, a  $q$ -plate is included before the GP lens in order to create a cylindrically polarized light beam, and the linear analyzer at  $45^\circ$  is kept before the CCD. In Figs. 7(c) and 7(d)  $q$ -plates with values  $q=1/2$  and  $q=1$  were employed. These  $q$ -plates are illuminated with linearly polarized light, thus a linear vector beam is generated. Now the interference pattern describes a clockwise spiral rotation due to the opposite sign of the topological charge in the RCP and LCP beams splitting at the GP lens. Note that the number of fringes starting at the singularity on axis is four times the  $q$ -value, i.e., two in Fig. 7(c) and four in Fig. 7(d).

Finally, the last column in Fig. 7 shows the interference pattern observed when two  $q$ -plates, combined with regular HWRs, are inserted before the GP lens. As shown in Ref. [25], two  $q$ -plates with a HWR in-between make an effective  $q$ -plate with a  $q$ -value equal to the addition of the individual  $q$ -values. Therefore, when inserting a HWR between the two  $q$ -plates of  $q=1/2$  and  $q=1$ , we are generating an equivalent  $q$ -plate of  $q=3/2$ . The interference pattern in Fig. 7(e) shows this situation, where a singularity of greater diameter is observed, with six clockwise spiral interference fringes originating from it.

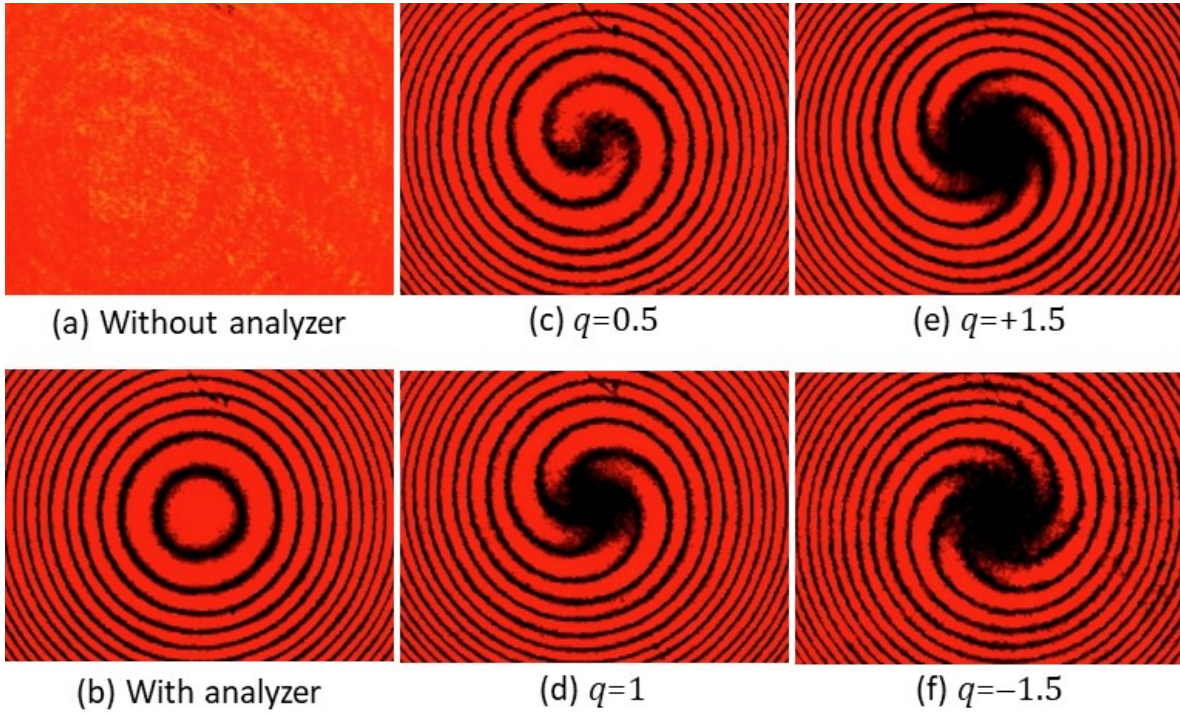


Fig. 7. Experimental interference patterns at the intermediate plane (IP) in between the two foci (see Fig. 2), in all cases the system is illuminated with linearly polarized light at  $45^\circ$ . (a) Case with no analyzer and no  $q$ -plate; (b) case with linear analyzer at  $45^\circ$  and no  $q$ -plate; In cases (c) to (f) the analyzer remains and a  $q$ -plate is added before the GP lens: (c) case  $q=1/2$ ; (d) case with  $q=1$ ; (e) case with  $q=1/2 - \text{HWR} - q=1$ ; (f) case with  $\text{HWR} - q=1/2 - \text{HWR} - q=1 - \text{HWR}$ .

Again, following Ref. [25], when a  $q$ -plate is inserted in between two HWPs, the system is equivalent to an effective  $q$ -plate with opposite  $q$ -value. Therefore, by adding two HWPs on each side of the previous system used in Fig. 7(e) yields a  $q$ -plate of  $q=-3/2$ . The interference pattern in Fig. 7(f) verifies this situation. We can see that the spiral pattern is equivalent to that in Fig. 7(e), again with six fringes originating from the singularity, but now the spiral rotates counter-clockwise, revealing the change in sign of the topological charge.

In these experiments that combine two  $q$ -plates, it is crucial to achieve a perfect alignment of the centres of the  $q$ -plates and the centre of the GP lens. This is illustrated in the video included as supplementary material. It shows initially the interference pattern generated by the GP lens, as shown in Fig. 7(b). However, at both sides of the interference centre, the two singularities caused by the  $q$ -plates, which are now misaligned, are clearly visible. The file video1 shows how the regular interference pattern becomes the spiral interference pattern as the  $q$ -plates are aligned correctly.

Let us remark that this interference pattern can also be used to identify the input vector beam of a given order. This is illustrated in Fig. 8 where, as an example, we select the four standard linear first-order vector beams: radial, azimuthal, and the two slanted polarizations. They all lie on the equator of the first-order Poincaré sphere [27] and

therefore they yield an equally intense focalization in the two foci of our system since they all have equally intense RCP and LCP components. However, these four vector beams differ in their relative phase between the RCP and LCP components. This is clearly visible in the intermediate interference pattern, as we discuss below.

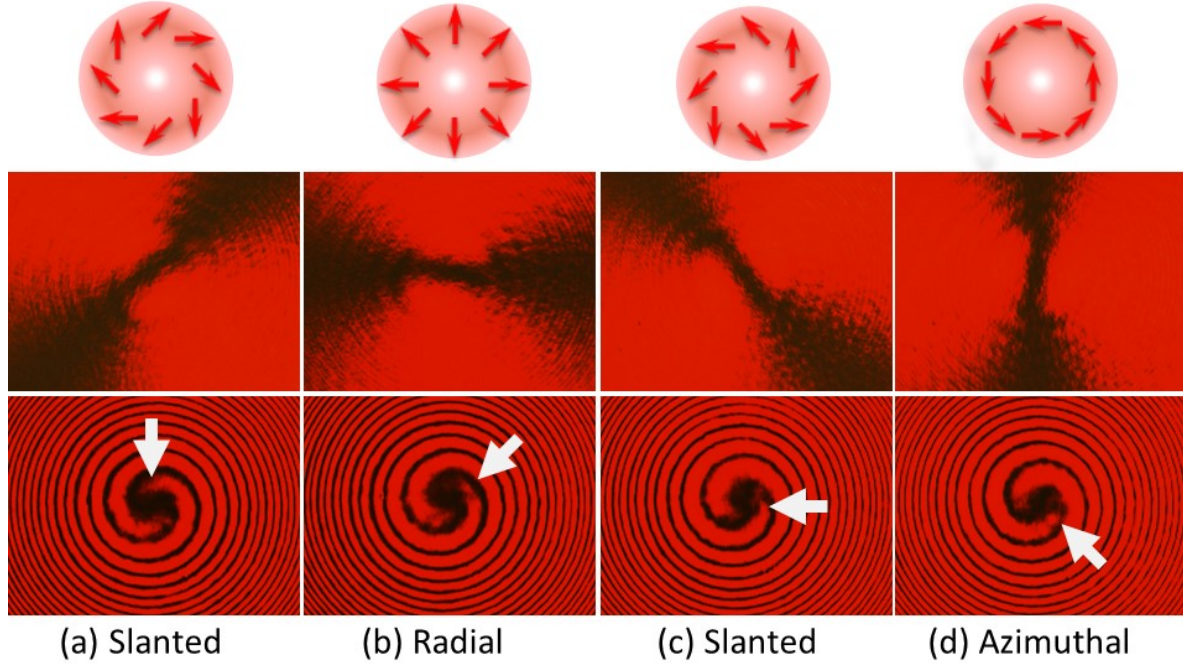


Fig. 8. Experimental results when the system includes the  $q$ -plate with  $q=1/2$  illuminated with linearly polarized light at four different angles to generate different linear first-order vector beams: (a) Slanted; (b) Radial; (c) Opposite slanted and (d) Azimuthal. The analyzer is always oriented vertically. The middle row shows the pattern behind the  $q$ -plate. The bottom row shows the Interference at the intermediate plane (IP). The white arrow indicates the position where the bright fringe starts.

We have generated the four linear first-order vector beams by illuminating the  $q=1/2$   $q$ -plate with input linear polarization oriented vertically, horizontally and at  $\pm 45^\circ$ . The images in the middle row shows the intensity pattern captured behind the  $q$ -plate, which identifies generated vector beam by the dark line that appears for the areas where the polarization is orthogonal to the analyzer transmission axis [7]. The bottom row displays the corresponding interference pattern captured at the intermediate plane. Note how the fringes in the spiral pattern are shifted by phase steps of  $\pi/2$ . These shifts are clearly visible as rotations of the spiral pattern in the center of the interferogram. A second file video2 illustrates how both patterns rotate.

## 5. Conclusions

In summary, we have combined two geometric phase optical elements that enable to manipulate the polarization and phase properties of a polarized light beam. We first

demonstrated the selection of polarization by a GP lens, showing their dual circular-polarization-based split properties. We combined the GP lens with a telescope to design an optical system with two real foci of equal magnification. This ensures a direct comparison of these two real foci, thus making a simple task to compare the OAM content on each spin component.

Then, we incorporated  $q$ -plate elements before the optical lens system. The  $q$ -plates transfer orbital angular momentum (OAM) to the input beam, which is easily visualized in the doughnut shape of the corresponding focalizations. Finally, we used the intermediate plane in between the two foci to clearly display the interference pattern of the two vortex beams constituent of the input vector beam. The different spiral interferograms reveal the different characteristics of the input vector beams.

The proposed optical system based on the use of the GP lens and the telescopic system is a simple and useful method to characterize vector beams, since it splits longitudinally the circular polarization components and focuses them into different axial planes. The shape and size of the focalizations obtained at the two foci indicate the topological charge encoded on each circular polarization component. The interference pattern at the intermediate plane reveal the sign and value of the vector beams topological charge. It also reveals the relative phase between the RCP and LCP components, and consequently, the shift in the fringes makes possible to identify the vector beam of a given order.

These experiments show the potential of the GP lens as a new element for the design of optical lens systems with different polarization properties that could be exploited in applications that require polarization splitting. For instance, the proposed optical set-up could benefit the research on the spin-Hall effect of light, which has been proposed for optical manipulation and trapping. We have shown that this system discriminates unambiguously between the four fundamental vector modes (radial, azimuthal, and the two slanted). Nevertheless, let us point out that, as presented, it would not be able to separate spatially these four fundamental vector modes, as it is required in vector beam based optical communications. For that purpose, the proposed system could be combined with a specially designed polarization vortex diffraction grating, as those proposed in [30,31].

#### **Acknowledgements:**

We thank Dr. José Luis Martínez-Fuentes for useful suggestions about the optical system.

#### **Fundings:**

This work has been financed by Generalitat Valenciana, Conselleria d'Educació, Investigació, Cultura i Esport (PROMETEO-2017-154) and by Ministerio de Economía, Industria y Competitividad of Spain and European Union (MIMECO/FEDER funds, "Una manera de hacer Europa" (grant FIS2015-66328-C3-3-R). A. Vargas and F. Torres-Ruiz

acknowledge support from CONICYT/FONDECYT (grant 1151290). A. Cofré acknowledges Generalitat Valenciana for a grant of the Santiago Grisolia Program, Ref. 2015/073.

## References

- [1]. Kim J, Li Y, Miskiewicz MN, Oh C, Kudenov MW, Escuti MJ., Fabrication of ideal geometric-phase holograms with arbitrary wavefronts. *Optica* 2015; **2**:958- 64.
- [2]. De Sio L, Roberts DE, Liao Z, Nersisyan S, Uskova O, Wickboldt L, Tabiryan N, Steeves DM, Kimball BR. Digital polarization holography advancing geometrical phase optics. *Opt. Express* 2016; **24**:18297-306.
- [3]. Mueller JPB, Rubin NA, Devlin RC, Groever B, Capasso F. Metasurface polarization optics: independent phase control of arbitrary orthogonal states of polarization. *Phys. Rev. Lett.* 2017; **118**: 113901.
- [4]. Beresna M, Gecevičius M, Kazansky PG, Gertus T. Radially polarized optical vortex converter created by femtosecond laser nanostructuring of glass. *Appl. Phys. Lett.* 2011; **98**: 201101.
- [5]. Yu N, Aieta F., Genevet P, Kats MA, Gaburro Z, Capasso F. A broadband, background-free quarter-wave plate based on plasmonic metasurfaces. *Nano Lett.* 2012; **12**: 6328–33.
- [6]. Slussarenko S, Murauski A, Du T, Chigrinov V, Marrucci L, Santamato E. Tunable liquid crystal  $q$ -plates with arbitrary topological charge. *Opt. Express* 2011; **19**: 4085-90.
- [7]. Davis JA, Hashimoto N, Kurihara M, Hurtado E, Pierce M, Sánchez-López MM, Badham K, Moreno I. Analysis of a segmented  $q$ -plate tunable retarder for the generation of first-order vector beams. *Appl. Opt.* 2015; **54**: 9583-90.
- [8]. Marrucci L, Manzo C, Paparo D. Optical spin-to-orbital angular momentum conversion in inhomogeneous anisotropic media. *Phys. Rev. Lett.* 2016; **96**: 163905.
- [9]. Shu W, Ling X, Fu X, Liu Y, Ke Y, Luo H. "Polarization evolution of vector beams generated by  $q$ -plates. *Photonics Res.* 2017; **5**: 64-72.
- [10]. Moreno I, Sánchez-López MM, Badham K, Davis JA, Cottrell DM. Generation of integer and fractional vector beams with  $q$ -plates encoded onto a spatial light modulator. *Opt. Lett.* 2016; **41**: 1305-8.
- [11]. Samlan CT, Viswanathan NK. Generation of vector beams using a double-wedge depolarizer: Non-quantum entanglement. *Opt. Laser Eng.* 2016; **82**: 135–40.
- [12]. Dong X, Geng T, Chen J, Zhuang S. A generation method of tunable cylindrical vector ring beam. *Opt. Laser Eng.* 2012; **50**: 1823-27.
- [13]. Hasman E, Kleiner V, Biener G, Niv A. Polarization dependent focusing lens by use of quantized Pancharatnam–Berry phase diffractive optics. *Appl. Phys. Lett.* 2003; **82**: 328-30.

- [14]. Chen X, Huang L, Mühlenbernd H, Li G, Bai B, Tan Q, Jin G, Qiu CW, Zhang S, Zentgraf T. Dual polarity plasmonic metalens for visible light. *Nat. Commun.* 2012; **3**: 1198.
- [15]. Wang S, Wang X, Kan Q, Ye J, Feng S, Sun W, Han P, Qu S, Zhang Y. Spin-selected focusing and imaging based on metasurface lens. *Opt. Express* 2015; **23**: 26434-41.
- [16]. Khorasaninejad M, Chen WT, Zhu AY, Oh J, Devlin RC, Roques-Carmes C, Mishra I, Capasso F. Visible wavelength planar metalenses based on titanium dioxide. *IEEE J. Sel. Topics Quant. Electron.* 2017; **23**: 4700216.
- [17]. Gao K, Cheng HH, Bhowmik A, McGinty C, Bos P. Nonmechanical zoom lens based on the Pancharatnam phase effect. *Appl. Opt.* 2016; **55**: 1145-50.
- [18]. Li C, Zhao S. Efficient separating orbital angular momentum mode with radial varying phase. *Photonics Res.* 2017; **5**: 267-70.
- [19]. Trichili A, Rosales-Guzmán C, Dudley A, Ndagano B, Ben Salem B, Zghal M, Forbes A. Optical communication beyond orbital angular momentum. *Sci. Rep.* 2016; **6**: 27674.
- [20]. Milione G, Nguyen TA, Leach J, Nolan DA, Alfano RR. Using the nonseparability of vector beams to encode information for optical communication. *Opt. Lett.* 2015; **40**: 4887-90.
- [21]. Li Y, Liu Y, Ling X, Yi X, Zhou X, Ke Y, Luo H, Wen S, Fan D. Observation of photonic spin Hall effect with phase singularity at dielectric metasurfaces. *Opt. Express* 2015; **23**: 1767-74.
- [22]. Ling X, Zhou X, Yi X, Shu W, Liu Y, Chen S, Luo H, Wen S, Fan D. Giant photonic spin Hall effect in momentum space in a structured metamaterial with spatially varying birefringence. *Light: Sci. & Appl.* 2015; **4**: e290.
- [23]. Liu S, Li P, Zhang Y, Gan X, Wang M, Zhao J. Longitudinal spin separation of light and its performance in three-dimensionally controllable spin-dependent focal shift. *Sci. Rep.* 2016; **6**: 20774.
- [24]. Saleh BEA, Teich MC. *Fundamentals of Photonics*. New York: John Wiley & Sons; 1991.
- [25]. S. Delaney, M. M. Sánchez-López, I. Moreno, and J. A. Davis, "Arithmetic with  $q$ -plates," *Appl. Opt.* **56** (3), 596- 600 (2017).
- [26]. Moreno I, Davis JA, Ruiz I, Cottrell DM. Decomposition of radially and azimuthally polarized beams using a circular-polarization and vortex-sensing diffraction grating. *Opt. Express* 2010; **18**: 7173-83.
- [27]. Milione G, Sztul HI, Nolan DA, Alfano RR. Higher-order Poincaré sphere, Stokes parameters, and the angular momentum of light. *Phys. Rev. Lett.* 2011; **107**: 053601.
- [28]. Liu Z, Liu Y, Ke Y, Liu Y, Shu W, Luo H, Wen S. Generation of arbitrary vector vortex beams on hybrid-order Poincaré sphere. *Photonics Res.* 2017; **5**: 15-21.
- [29] Gossman D, Perez-Garcia B, Hernandez-Aranda RI, Forbes A. Optical interference with digital holograms. *Am. J. Phys.* 2016; **84**: 508-16.

- [30] Moreno I, Davis, JA, Badham K, Sánchez-López MM, Holland JE, Cottrell DM. Vector beam polarization state spectrum analyzer. *Sci. Rep.* 2017; **7**: 2216.
- [31] Rosales-Guzmán C, Bhebhe N, Forbes A. Simultaneous generation of multiple vector beams on a single SLM. *Opt. Express* 2017 25: 25697-706.
- [32] Moreno I, Ferreira C, Fractional Fourier transform and Geometrical Optics. In: *Advances in Imaging and Electron Physics* 2010; **161**: 89-146.

## Appendix: Analysis of the imaging system

The use of the telescopic system to create the two real foci is though limited. For this analysis, we use the ABCD ray matrix approach [32]. The telescopic system is composed of two positive lenses  $L_1$  and  $L_2$ , with focal lengths  $f_1$  and  $f_2$  respectively. The back focal plane of  $L_1$  is made coincident with the front focal plane of  $L_2$ . Therefore, the ABCD ray matrix for the telescope is given by:

$$\mathbf{M}_{TEL} = \begin{pmatrix} 1 & 0 \\ -\frac{1}{f_2} & 1 \end{pmatrix} \cdot \begin{pmatrix} 1 & f_1 + f_2 \\ 0 & 1 \end{pmatrix} \cdot \begin{pmatrix} 1 & 0 \\ -\frac{1}{f_1} & 1 \end{pmatrix} = \begin{pmatrix} -M & D \\ 0 & -\frac{1}{M} \end{pmatrix} \quad (4)$$

where  $M = f_2 / f_1$  denotes the magnification, and  $D = f_1 + f_2$  denotes the distance between lenses  $L_1$  and  $L_2$ .

If an object plane located a distance  $X$  in front of lens  $L_1$  is to be imaged onto an image plane at a distance  $Y$  behind the lens  $L_2$ , the ABCD ray matrix for the system is:

$$\mathbf{M}_{IMA} = \begin{pmatrix} 1 & X \\ 0 & 1 \end{pmatrix} \cdot \begin{pmatrix} -M & D \\ 0 & -\frac{1}{M} \end{pmatrix} \cdot \begin{pmatrix} 1 & Y \\ 0 & 1 \end{pmatrix} = \begin{pmatrix} -M & D - MX - \frac{Y}{M} \\ 0 & -\frac{1}{M} \end{pmatrix} \quad (5)$$

where the imaging condition  $B=0$  leads to the following relation

$$Y = M(D - MX) \quad (6)$$

Since we want to have real images, we must impose the condition  $Y \geq 0$ . This is accomplished whenever the condition

$$X \leq \frac{D}{M} = f_1 \left( 1 + \frac{f_1}{f_2} \right) \quad (7)$$

is fulfilled. This condition limits the farthest point that can be imaged with the telescope while providing a real image.

The above-mentioned farthest point limits the distance the telescope can be placed behind the GP lens to obtain two real foci for the complete system composed by the GP lens and the telescope. Different situations are illustrated in Fig. 9. Figure 9(a) corresponds to the case where the real image is located at the closest point, i.e.,  $Y=0$ . In this situation, the first lens of the telescope creates the intermediate image onto the location of the second lens. This case corresponds to the farthest real object that can be imaged onto a real image behind the telescope, according to the limit in Eq. (7). For the

telescope with two equal lenses illustrated in Fig. 9, the farthest object is located at a distance  $X=2f$ .

Figure 9(b) shows the case corresponding to a real object located on the front focal plane of lens  $L_1$ , which is then imaged on the back focal plane of lens  $L_2$ . Figure 9(c) illustrates the limiting case for a real object, achieved when  $X=0$ , i.e., the object is right on the location of the first lens. In the case of the telescope with equal lenses, the real image appears at a distance  $Y=2f$ , according to Eq. (6). Finally, Fig. 8(d) shows the case where a virtual object is imaged. In this case, the image plane appears farther apart from the back focal plane of lens  $L_2$ . The case illustrated in Fig. 8(d) corresponds to a distance  $X=-f$  (a virtual object point located at the back focal plane of lens  $L_1$ ), and the final image appears at a distance  $Y=3f$ .

These limits impose the conditions where we can image the two focal planes of the GP lens with a real image. Let  $F$  denote the focal length of the GP lens, i.e. it creates two foci (real and virtual at distances  $\pm F$  from the GP lens. If the telescope system is placed right behind the GP lens (Fig. 8(a)), then the real focus of the GP lens becomes a virtual object for the telescope with  $X_2=-F$ , (therefore always fulfilling condition (6)) and the telescope provides a final focal plane  $F_2$  located a distance  $Y_2=M(D+MF)$  from lens  $L_2$ . On the contrary, the virtual focus of the GP lens is a real object for the telescope, with  $X_1=+F$ , and therefore the focal plane  $F_1$  is located a distance  $Y_1=M(D-MF)$  which is positive provided the limiting condition in Eq. (6).

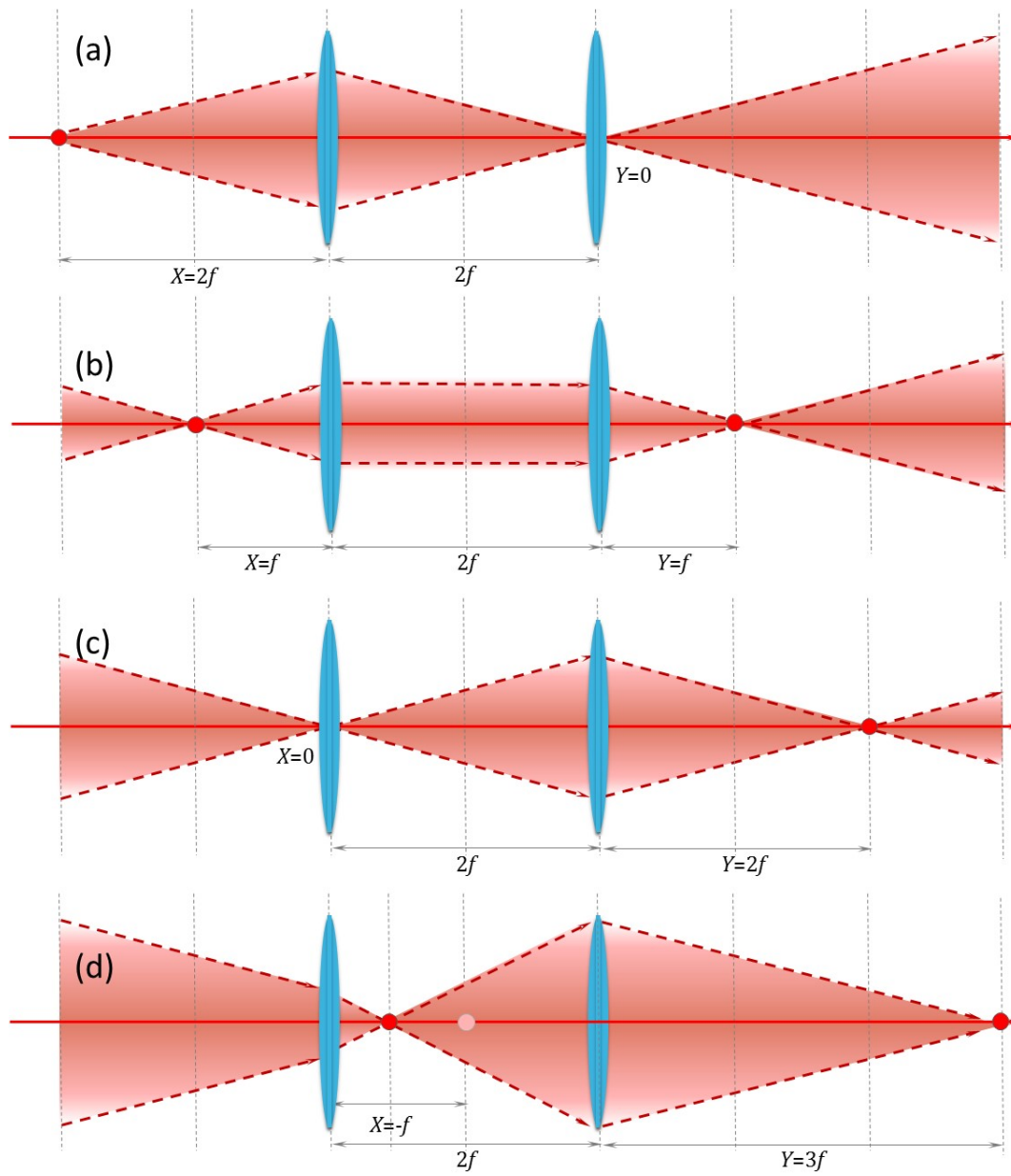


Fig. 9. Different cases illustrating the real imaging condition with the telescope system. For simplicity,  $f_1=f_2\equiv f$  has been selected. (a) Closest real image ( $Y=0$ ); (b) Focus to focus propagation; (c) Closest real object and (d) a case with virtual object.